A Parametric Study of Cathode Catalyst Layer Structural Parameters on the Performance of a PEM Fuel Cell

N. Khajeh-Hosseini D.,[1] M. J. Kermani,[1,*] D. Ghadiri Moghaddam[1] and   J. M. Stockie[2]

[1]Department of Mechanical Engineering, Energy Conversion Research Laboratory, Amirkabir University of Technology (Tehran Polytechnic), Tehran, Iran 15875–4413
[2]Department of Mathematics, Simon Fraser University, Burnaby, BC, Canada, V5A 1S6

Abstract

This paper is a computational study of the cathode catalyst layer (CL) of a proton exchange membrane fuel cell (PEMFC) and how changes in its structural parameters affect performance. The underlying mathematical model assumes homogeneous and steady-state conditions, and consists of equations that include the effects of oxygen diffusion, electrochemical reaction rates, and transport of protons and electrons through the Nafion ionomer (PEM) and solid phases. Simulations are concerned with the problem of minimizing activation overpotential for a given current density. The CL consists of four phases: ionomer, solid substrate, catalyst particles and void spaces. The void spaces are assumed to be fully flooded by liquid water so that oxygen within the CL can diffuse to reaction sites via two routes: within the flooded void spaces and dissolved within the ionomer phase. The net diffusive flux of oxygen through the cathode CL is obtained by incorporating these two diffusive fluxes via a parallel resistance type model. The effect of six structural parameters on the CL performance is considered: platinum and carbon mass loadings, ionomer volume fraction, the extent to which the gas diffusion layer (GDL) extends into the CL, the GDL porosity and CL thickness. Numerical simulations demonstrate that the cathode CL performance is most strongly affected by the ionomer volume fraction, CL thickness and carbon mass loading. These results give useful guidelines for manufactures of PEMFC catalyst layers.

Keywords: PEM fuel cell; catalyst layer; macro-homogeneous model; numerical simulations; sensitivity study

*Corresponding Author: Assistant Professor and Head of Energy Conversion Research Laboratory, Tel.: +98 21 6454 3421; Fax: +98 21 6641 9736. *E-mail address*: mkermani@aut.ac.ir (M.J. Kermani).

1 Introduction

In a proton exchange membrane fuel cell (or PEMFC), electrical energy is generated directly through an electrochemical reaction between oxygen and hydrogen. PEMFCs have high power density, quick start-up times, and produce power with theoretically zero emissions. These advantages make them one of the most serious alternatives to replace the internal combustion engines. However, even with recent advances in materials and optimization of fuel cell processes, commercialization of PEMFCs is still being delayed pending further improvements in performance and cost.

The key electrochemical reaction in a PEMFC occurs at the cathode catalyst layer (or CL) where oxygen and hydrogen are combined to generate an electrical current at a rate directly proportional to the electrochemical reaction rate. The rate of reaction is mainly dependent on CL structural parameters related to the composition and distribution of CL materials as well as how the CL is synthesized. A robust and reliable PEMFC performance analysis requires a thorough understanding of CL performance through extensive parametric studies. Experimental investigations are indispensible in this regard but they can be very time-consuming and costly, particularly if many parameters are involved (see [11] and [12]). Furthermore, it can be quite difficult to correlate the usually sparse experimental data to specific aspects of CL structure. Therefore, numerical simulations can be very useful in predicting and optimizing CL performance, especially in the early stages of design.

Models for the cathode CL can be broadly classified into three different categories based on their level of complexity: interface models, macro-homogeneous models, and agglomerate models. Each model has its advantages and disadvantages that we next discuss briefly:

Interface models were the first applied to modelling the entire fuel cell, and they have been used commonly since then because of their simplicity. The CL is treated as an infinitely thin layer and no attempt is made to capture spatial variations in solution profiles. Consequently, these models are posed in terms of averaged transport parameters and so provide only limited guidance on microstructure and performance optimization. On the other hand, interface models are computationally efficient and so are are very suitable for multidimensional computations and parametric studies of the entire fuel cell. For example, Berning and Djilali [1] developed a 3D, non-isothermal model using a CFD approach, investigating the effects on fuel cell performance of parameters such as GDL porosity and thickness, and channel width. Lum and McGuirk [2] performed a similar study that examined the influence of permeability and oxidant concentration as well as geometrical parameters.

Macro-homogeneous models (also called "pseudo-homogeneous" models) were first introduced by Tiedemann and Newman [3] and consider the CL as a layer of finite thickness, with averaged transport coefficients describing the effect of variations in compositional parameters describing platinum catalyst, carbon support, solid GDL matrix, and electrolyte materials. Marr and Li [4]

2

Manuscript Submitted to Journal of Applied Electrochemistry
Khajeh-Hosseini D., Kermani, Ghadiri Moghaddam and Stockie

used this type of model to investigate the influence of CL composition and especially platinum loading on CL performance. They also provided experimental evidence that the CL can be flooded with water even at very low current densities. You and Liu [5] performed simulations using a control volume approach to study the effect of membrane conductivity and CL porosity. Du et al. [6] performed a more extensive parametric study based on a macrohomogeneous model in which they assumed that oxygen diffuses to active catalyst sites solely in the gas phase, while more recent work suggests that significant oxygen transport also occurs in dissolved phase within the ionomer.

Agglomerate models represent the most sophisticated approach, taking into account both the composition and structural distribution of CL materials. Particles consisting of platinum plus carbon support (Pt/C) are grouped in small agglomerates that are surrounded by and bonded together with electrolyte and GDL material. A relatively uniform distribution of intra- and inter-agglomerate materials is vital in order to correlate agglomerate structure with performance. Beginning with the pioneering work of Ridge et al. [7], many other agglomerate models have been developed especially in recent years. Secanell et al. [8] used parametric studies to determine optimal values of platinum loading, Pt/C ratio, electrolyte volume fraction and the GDL porosity, which they also showed depend on operating conditions. Shah et al. [9] developed a 1D transient model for the entire membrane-electrode assembly (MEA) of a PEMFC, considering effects of humidification, temperature, pore size and GDL contact angle. Wang et al. [10] studied the effect of void fraction, inflow relative humidity, and the net water transport, and showed that low humidity operation can benefit cell performance by reducing oxygen transport at high current densities.

Among the three types of models, the thin interface approach is the simplest and the agglomerate approach is the most complex. The macro-homogeneous models fall somewhere in between, and have the advantage that they can provide reliable results at low and medium cell current densities [8].

In order that a catalyst layer model is capable of reliably predicting performance, it is essential that it captures the complex multi-material structure of the CL. Agglomerate models seem to provide the best fit to experimental results [13]; however, it is still unclear how the agglomerates are formed and how they are defined within the complex random multi-material morphology of the porous CL matrix. Taking into consideration both these uncertainties and the greater complexity of the agglomerate model, the macro-homogeneous models stand out as a more desirable alternative to obtain detailed information about the correlations between CL structure and performance [8].

In this paper a steady-state, macro-homogeneous CL model is used to study transport in the cathode catalyst layer within a medium range of current densities. The governing equations are a coupled system of ODEs that capture oxygen diffusion, electrochemical reactions, and the transport of electrons and protons. The equations are solved using a shooting algorithm that makes use of a Runge-

Kutta time-stepping technique to integrate the equations to steady state. Numerical simulations are used to study the dependence of PEMFC performance on six structural parameters: platinum and carbon mass loading, CL thickness, ionomer volume fraction, the extent of GDL penetration into the CL, and GDL porosity. Most other studies of CL performance have focused on a limited number of structural parameters (e.g., [1], [13]) whereas in the present study we consider a more extensive selection of parameters. The dependent variable is the activation overpotential and parametric studies are used to probe the effect of the structural parameters on the overpotential; in particular, minimizing the activation overpotential at a given cell current density is the goal of this study. The results give guidelines that should prove useful to MEA manufacturers.

2 The Model Description

A representative picture of the catalyst layer is shown schematically in Fig. 1. Hydrogen gas from the anode is split into electrons and protons at the anode side catalyst layer. The electrons are transferred through an external circuit to the cathode CL, while the protons move through the ionomer membrane to the cathode side. Oxygen is supplied on the cathode side where it diffuses in gas form through void spaces in the GDL to the GDL/CL interface.

The present study is concerned with what occurs once the three reacting species – oxygen gas, protons and electrons – reach the cathode CL. We assume the CL consists of four distinct regions (refer to Fig. 1): (1) catalyst clusters, consisting of platinum and carbon support; (2) Nafion ionomer phase; (3) solid GDL phase; and (4) void spaces. Oxygen diffuses in dissolved form through the flooded void spaces and the ionomer membrane. Hydrogen is transported as ions through through the ionomer phases, while electrons move only through the solid conductive phase. All three reacting species – O_2, H^+ and e^- – reach the reaction sites on Pt/C clusters where the electrochemical reaction

$$O_2 + 4H^+ + 4e^- \quad \to \quad 2H_2O + \text{ Heat} \tag{1}$$

takes place. As shown in Fig. 1, the materials lying on either side of the cathode CL (i.e. GDL and membrane) are designed such that they penetrate partially into the layer, which allows the reacting species ready access to reaction sites. We note that the ionomer membrane is a polymer (Nafion) whose ability to conduct protons increases with hydration level, and so maintaining sufficient hydration levels within the CL is essential.

3 Governing Equations

In the derivation of the equations to follow, we make a number of simplifying assumptions:
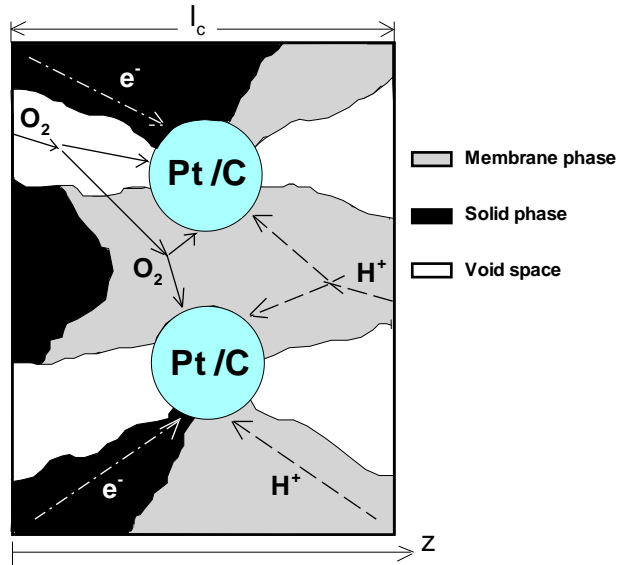
1. The problem is one–dimensional and steady.

Figure 1: Schematic of the cathode CL for a PEM fuel cell (adapted from [14]).

2. The CL is a macro-homogeneous medium consisting of the four components depicted in Fig. 1.

3. The GDL and membrane phases penetrate a well-defined distance into the CCL.

4. Operating pressure and temperature are constant.

5. Void spaces are fully flooded by liquid water.

The governing equations are split in two groups: algebraic equations governing CL composition, and differential equations governing transport.

3.1 Algebraic Equations Governing Composition

3.1.1 Phase compositions

We first define the following volume fractions:

- ε_c is the void volume fraction, or CL porosity.

- $L_{m,c}$ is the volume fraction of the ionomer phase.

- $L_{g,c}$ is the volume fraction of the GDL penetrating into the CL. Then the volume fraction of the solid portion of the GDL is

$$L_s = L_{g,c}(1 - \varepsilon_g), \tag{2}$$

where ε_g is the GDL porosity.

- $L_{Pt/C}$ is the volume fraction of the catalyst Pt/C particles.

The following equation governs the four corresponding volumes

$$V_{tot} = V_{m,c} + V_c + V_{Pt/C} + V_s, \tag{3}$$

where V_{tot} is the total CL volume. The volume fractions can then be written as

$$L_{m,c} = \frac{V_{m,c}}{V_{tot}}, \quad \varepsilon_c = \frac{V_c}{V_{tot}}, \quad L_{Pt/C} = \frac{V_{Pt/C}}{V_{tot}} \quad \text{and} \quad L_s = \frac{V_s}{V_{tot}}, \tag{4}$$

after which

$$L_{m,c} + L_{g,c}(1 - \varepsilon_g) + L_{Pt/C} + \varepsilon_c = 1. \tag{5}$$

The quantity $L_{Pt/C}$ in Eq. 5 can be expressed in terms of the mass loading of catalyst particles per unit area of the cathode. Consider the total volume of the CL, $V_{tot} = A \times l_c$, where A is the area of the cathode and l_c is the CL thickness. Keeping in mind that $V_{Pt/C} = V_{Pt} + V_C$, we may write

$$V_{Pt} = \frac{(\text{mass})_{Pt}}{\rho_{Pt}} \quad \text{and} \quad V_C = \frac{(\text{mass})_C}{\rho_C} \tag{6}$$

where ρ_{Pt} and ρ_C are the density of platinum and carbon repectively. Defining the mass loading of platinum and carbon per unit area of the cathode as

$$m_{Pt} \equiv \frac{(\text{mass})_{Pt}}{A} \quad \text{and} \quad m_C \equiv \frac{(\text{mass})_C}{A}, \tag{7}$$

we may write

$$L_{Pt/C} = \frac{m_{Pt}}{\rho_{Pt} l_c} + \frac{m_C}{\rho_C l_c}. \tag{8}$$

We then introduce the mass fraction of platinum to that of Pt/C particles,

$$f \equiv \frac{m_{Pt}}{m_{Pt} + m_C}, \tag{9}$$

where $f = 1$ for pure platinum and $f = 0$ for pure carbon. We substitute this expression along with Eqs. 8 into Eq. 5 to write the CL porosity as

$$\varepsilon_c = 1 - L_{m,c} - L_{g,c}(1 - \varepsilon_g) - \underbrace{\frac{m_{Pt}}{l_c} \left[\frac{1}{\rho_{Pt}} + \frac{1-f}{f} \frac{1}{\rho_C} \right]}_{=L_{Pt/C}}. \tag{10}$$

This expression will be used in the next section to determine the effective oxygen diffusion coefficient.
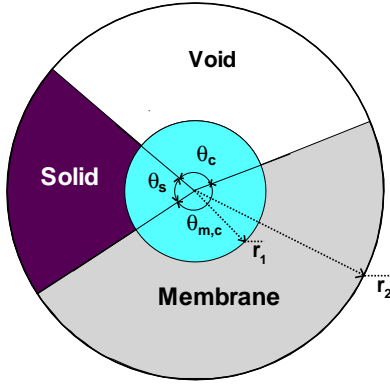
Figure 2: A cylindrical control volume element with the Pt/C particle located at the center of the element, surrounded by the void, solid and membrane phases.

3.1.2 Oxygen diffusion coefficient

An equivalent (effective) diffusion coefficient for the oxygen species is determined in this section. To this end, we model the diffusion of gaseous oxygen through a cylindrical control volume element of radius r_2 surrounding a single Pt/C particle with radius $0 < r_1 < r_2$, as shown in Fig. 2. The Pt/C particle is located at the center of the element and is surrounded by sectors containing the ionomer, solid and void phases.

The distribution of Pt/C clusters through the entire CL is random; hence, the homogeneity assumption is a reasonable one. Furthermore, the average diffusion lengths for the oxygen species through both the void and ionomer phases is equal to $(r_2 - r_1)$. According to the division of phases depicted in Fig. 2,

$$2\pi = \theta_{m,c} + \theta_c + \theta_s, \tag{11}$$

where $\theta_{m,c}$, θ_c and θ_s are the contact angles corresponding to ionomer, void and solid phases respectively. The corresponding volumes are

$$V_{m,c} = \frac{1}{2}\theta_{m,c}(r_2^2 - r_1^2)\,\ell \qquad V_c = \frac{1}{2}\theta_c(r_2^2 - r_1^2)\,\ell \qquad V_s = \frac{1}{2}\theta_s(r_2^2 - r_1^2)\,\ell \tag{12}$$

where ℓ is the out-of-plane depth of the cylindrical element. From Eq. 12, we then obtain the following identity:

$$\frac{V_{m,c}}{\theta_{m,c}} = \frac{V_c}{\theta_c} = \frac{V_s}{\theta_s} = \frac{1}{2}\left(r_2^2 - r_1^2\right)\ell. \tag{13}$$

Next, in analog with thermal resistance for heat conduction in cylinders [15], we write the diffusion resistance R as

$$R \equiv \frac{\ln\left(r_2/r_1\right)}{\theta\,D^{eff}\,\ell} \tag{14}$$

where θ is the contact angle and D^{eff} is an effective diffusion coefficient. Oxygen reaches Pt/C reaction sites by diffusing through two parallel routes – the ionomer phase and void spaces (which are fully flooded by liquid water). Using Eq. 14, we can write the diffusion resistances in the ionomer ($R_{m,c}$) and void (R_c) regions as

$$R_{m,c} = \frac{\ln(r_2/r_1)}{\theta_{m,c}\, D^{eff}_{O_2-m}\, \ell} \qquad \text{and} \qquad R_c = \frac{\ln(r_2/r_1)}{\theta_c\, D^{eff}_{O_2-w}\, \ell}, \tag{15}$$

where the effective diffusion coefficients (in units of $m^2\,s^{-1}$) are denoted by $D^{eff}_{O_2-m}$ in the membrane region and $D^{eff}_{O_2-w}$ in the water-flooded void region. According to [16], the effective diffusion coefficients can be expressed as

$$D^{eff}_{O_2-m} = L^{3/2}_{m,c}\, D_{O_2-m} \qquad \text{and} \qquad D^{eff}_{O_2-w} = \varepsilon_c^{3/2}\, D_{O_2-w}\,, \tag{16}$$

where D_{O_2-w} is a function of temperature (evaluated using Wilke-Chang equation [17], with the numerical value given in Table 2) and D_{O_2-m} is obtained by a curve fit to experimental data [18]

$$D_{O_2-m} = 1.4276 \times 10^{-11}\, T - 4.2185 \times 10^{-9}, \tag{17}$$

where the temperature T is measured in degrees Kelvin.

Using Eqs. 4, 11 and 13, the contact angle for each phase can be written in terms of species volume fractions as

$$\theta_{m,c} = \frac{L_{m,c}}{L_{m,c} + \varepsilon_c + L_s}\, 2\pi \qquad \text{and} \qquad \theta_c = \frac{\varepsilon_c}{L_{m,c} + \varepsilon_c + L_s}\, 2\pi\,, \tag{18}$$

following which the diffusion resistances can be obtained from Eqs. 15 as

$$R_{m,c} = \frac{L_{m,c} + \varepsilon_c + L_s}{L_{m,c}}\, \frac{\ln(r_2/r_1)}{2\pi\, D^{eff}_{O_2-m}\, \ell} \qquad \text{and} \qquad R_c = \frac{L_{m,c} + \varepsilon_c + L_s}{\varepsilon_c}\, \frac{\ln(r_2/r_1)}{2\pi\, D^{eff}_{O_2-W}\, \ell}\,. \tag{19}$$

We note that the diffusion resistance of each species is inversely proportional to its volume fraction. Treating the individual resistances in parallel, the equivalent total diffusion resistance R_{eq} is

$$\frac{1}{R_{eq}} = \frac{1}{R_{m,c}} + \frac{1}{R_c} \tag{20}$$

where we have defined

$$R_{eq} = \frac{\ln(r_2/r_1)}{2\pi D^{eff}_{O_2}\, \ell}. \tag{21}$$

The overall effective oxygen diffusion coefficient may then be found by combining Eqs. 19 and 21,

$$D^{eff}_{O_2} = D^{eff}_{O_2-m}\, \frac{L_{m,c}}{L_{m,c} + \varepsilon_c + L_s} + D^{eff}_{O_2-w}\, \frac{\varepsilon_c}{L_{m,c} + \varepsilon_c + L_s}, \tag{22}$$

in which the terms $L_{m,c}/(L_{m,c} + \varepsilon_c + L_s)$ and $\varepsilon_c/(L_{m,c} + \varepsilon_c + L_s)$ are, respectively, the volume fractions of the ionomer and void phases within the CL.

3.2 Governing Differential Equations

3.2.1 Oxygen diffusion

The transport due to diffusion of oxygen within the cathode CL is assumed to follow Fick's law [19]

$$N_{O_2} = -D_{O_2} \nabla C_{O_2}, \tag{23}$$

where N_{O_2}, D_{O_2} and C_{O_2} are, respectively, the superficial molar flux, bulk diffusion coefficient, and concentration of oxygen. The conservation of oxygen at steady state can be expressed as

$$\nabla \cdot N_{O_2} = R_{O_2}. \tag{24}$$

The consumption rate of oxygen per unit volume is denoted by R_{O_2}, which can be related to the protonic current density i by

$$R_{O_2} = -\frac{s}{nF} \nabla \cdot i, \tag{25}$$

where s is the stoichiometric coefficient, n is the number of electrons participating in the reaction, and F is the Faraday constant ($96485 \, Coulombs \, mol^{-1}$). According to Eq. 1, we have $s = 1$ and $n = 4$ after which Eq. 25 becomes

$$R_{O_2} = -\frac{1}{4F} \frac{di}{dz}, \tag{26}$$

where $\nabla \cdot i$ is replaced by di/dz in the present 1D study. We then combine this expression with Eqs. 23 and 24 to obtain

$$-D_{O_2}^{eff} \frac{d^2 C_{O_2}}{dz^2} = -\frac{1}{4F} \frac{di}{dz}, \tag{27}$$

where D_{O_2} is replaced by the effective diffusion coefficient $D_{O_2}^{eff}$ (determined in Sec. 3.1.2).

As indicated later in Eqs. 43–44, this last equation is subjected to the boundary condition $i = I_\delta$ and $dC_{O_2}/dz = 0$ at $z = l_c$ at the CL/membrane interface; therefore, Eq. 27 may be integrated once to obtain

$$\frac{dC_{O_2}}{dz} = \frac{i - I_\delta}{4F D_{O_2}^{eff}}. \tag{28}$$

3.2.2 Electrochemical reaction rate

The electrochemical reaction rate is determined by the Butler-Volmer equation [19]

$$\frac{di}{dz} = a \, i_0 \left[\exp\left(\frac{\alpha_c F}{RT} \eta_{act} \right) - \exp\left(-\frac{\alpha_a F}{RT} \eta_{act} \right) \right], \tag{29}$$

where i_0 is the exchange current density (determined experimentally for smooth-surface reaction sites), α_c and α_a are the cathodic and anodic transfer coefficients, and a is the specific area that takes into account the roughness of the reaction sites. The quantity a may be expressed as

$$a \equiv \frac{(\,\text{area}\,)_{RS}}{(A \times l_c)}, \tag{30}$$

where $(\text{area})_{RS}$ is the true area of reaction sites. Then, defining A_s to be the reaction surface area per unit mass of the platinum (in units of $m^2\,kg^{-1}$),

$$A_s \equiv \frac{(\text{area})_{RS}}{(\text{mass})_{Pt}},\tag{31}$$

and we may then write

$$A_s = \frac{a\,l_c}{m_{Pt}} \quad \text{or} \quad a = \frac{m_{Pt}}{l_c}A_s\,.\tag{32}$$

A curve fitting procedure is employed in Ref. [20] to approximate A_s in terms of the platinum mass fraction f according to

$$A_s = (227.79f^3 - 158.57f^2 - 201.53f + 159.5) \times 10^3\,.\tag{33}$$

In Eq. 29, i_0 is the exchange current density which is usually expressed in terms of a reference exchange current density $i_{0,ref}$ and reference concentration $C_{O_2,ref}$ [21] by

$$i_0 = i_{0,ref}\left(\frac{C_{O_2}}{C_{O_2,ref}}\right)^{\gamma_{O_2}},\tag{34}$$

where γ_{O_2} is the reaction order for the oxygen (and we take $\gamma = 1$ as recommended by Newman and Thoma-Alyea [22]. The ratio $\left(C_{O_2}/C_{O_2,ref}\right)^{\gamma_{O_2}}$ in Eq. 34 is in fact a correction factor for the deviation of concentration from the reference state. The reference exchange current density $i_{0,ref}$ from Eq. 34 (in $A\,m^{-2}$) is obtained from another curve fit to the experimental data provided in Ref. [18],

$$i_{0,ref} = 10^{0.03741T - 16.96}\,,\tag{35}$$

where T is the temperature in degrees Kelvin. Refer to Table 2 for values of the parameters appearing in the above equations.

3.2.3 Activation overpotential

The activation overpotential within the CL is caused by ohmic losses due to the protonic resistance in the ionomer phase and electrical resistance in the solid phase, according to [4]

$$\frac{d\eta_{act}}{dz} = \frac{i}{\kappa^{eff}} + \frac{i - I_\delta}{\sigma^{eff}}\,.\tag{36}$$

The effective protonic conductivity κ^{eff} can be related to its bulk value κ and the ionomer volume fraction via [16]

$$\kappa^{eff} = (L_{m,c})^{3/2}\,\kappa\,.\tag{37}$$

Similarly, the effective electronic conductivity may be written as

$$\sigma^{eff} = (1 - L_{m,c} - \varepsilon_c)^{3/2}\sigma\,.\tag{38}$$

Eqs. 28, 29 and 36 comprise a coupled system of nonlinear ODE's in the unknowns C_{O_2}, i and η_{act} that govern transport of oxygen, protons and electrons within the cathode CL.

4 Boundary Conditions

In order to obtain a well-posed problem, we must supplement the equations derived in the previous section with a number of boundary conditions which we describe next.

- **At the GDL/CL interface, z = 0**: Oxygen enters the CL pores from the GDL, and since the pores are assumed to be flooded with liquid water, the oxygen passes through the GDL/CL interface at $z = 0$ by first dissolving in water. The oxygen concentration at the interface is therefore determined using Henry's Law

$$C_{O_2}|_{z=0} = \frac{P_{O_2}}{H_{O_2}}, \tag{39}$$

where the oxygen partial pressure

$$P_{O_2} = x_{O_2} P, \tag{40}$$

x_{O_2} is the oxygen mole fraction, and P is the gas mixture pressure at the GDL/CL interface. The Henry constant H_{O_2} (in $atm\,m^3\,mol^{-1}$) is typically assumed to be a function of temperature [21] according to

$$H_{O_2} = 1.33 \exp\left(-\frac{666}{T}\right), \tag{41}$$

where T is measured in degrees Kelvin. Because the GDL is very thin, the pressure conditions at the GDL/CL interface are set to the cathode channel values, which we take to be $x_{O_2} = 0.21$ and $P = 5\,atm$.

The boundary condition for the protonic current density comes from the assumption that all protons are consumed before they reach the GDL/CL boundary, so that

$$i|_{z=0} = 0. \tag{42}$$

- **At the CL/membrane interface, z = l_c**: The protonic current density at the membrane approaches its ultimate value (i.e., the cell current density, I_δ), so that

$$i|_{z=l_c} = I_\delta. \tag{43}$$

Also, oxygen cannot reach this boundary because it is totally consumed within a narrow band in the vicinity of the GDL, so that

$$-\left.\frac{dC_{O_2}}{dz}\right|_{z=l_c} = 0. \tag{44}$$

5 Solution Procedure

The ODEs consisting of Eqs. 28, 29 and 36 along with boundary conditions Eqs. 39, 42–44 represent a two-point boundary value problem. We employ a shooting method in which a guess is made for $\eta_{act}|_{z=0}$ at the GDL/CL interface, and then we iterate on the solution until $i \to I_\delta$ at $z = l_c$. A Newton-Raphson method has also been used to speed up the convergence of the iteration [23].

6 Results

We now perform a number of simulations with the model just described, beginning with set of "base case" parameters presented in Table 2, and with four different values of the cell current density: $I_\delta = 50, 100, 200$ and 500 $mA\ cm^{-2}$. The results are depicted in Fig. 3 as plots of protonic current density i, oxygen concentration C_{O_2}, and activation overpotential η_{act}. The dissolved oxygen concentration is depleted rapidly in the vicinity of the GDL due to the fast oxygen reduction reaction in this region leading to formation of a thin boundary layer. In particular, at cell current densities of $I_\delta > 50$ $mA\ cm^{-2}$, the dissolved oxygen can only penetrate a very small distance into the CL; in other words, at these higher current densities only a small percentage of the catalyst layer is utilized. These predictions confirm the statement of Bernardi and Verbrugge [24] that most of the reaction occurs in first few microns bordering the GDL. The protonic current density profile in Fig. 3 for $I_\delta < 50\ mA\ cm^{-2}$ suggests that mass transport limitations do not seriously affect the solution; however, as I_δ increases, the oxygen transport becomes more important and the majority of current production shifts toward the GDL side of the catalyst layer. These results are in agreement with those of [25] and [26].

6.1 Validations

Next, we perform comparisons of our model with the experiments of Ticianelli et al. [11] and the CFD-based simulations of Khakbaz-Baboli and Kermani [27]. These comparisons are reported in terms of polarization curves (plots of voltage versus current) in which the cell voltage V_{cell} is calculated using [27]

$$V_{cell} = E_{rev} - \eta_{act} - RI_\delta, \tag{45}$$

where R is the specific resistance of the cell and E_{rev} is the reversible cell voltage [28]

$$E_{rev} = 1.229 - 0.85 \times 10^{-3}\left(T - 298.15\right) + 4.31 \times 10^{-5}T\left[\ln(P_{H_2}) + 1/2\ln(P_{O_2})\right]. \tag{46}$$

The quantities P_{H_2} and P_{O_2} are the partial pressures of hydrogen and oxygen respectively, which are obtained at total pressure of 5 atm with 100% relative humidity.

We employ the base case parameters from Table 2, except that the Ticianelli et al. comparison uses $m_{Pt} = 0.35\ mg\ cm^{-2}$ and $R = 0.225\ \Omega\ cm^{-2}$, while the Khakbaz-Baboli and Kermani comparison uses $m_{Pt} = 0.35\ mg\ cm^{-2}$, $T = 50^oC$ and $R = 0.47\ \Omega\ cm^{-2}$. In both cases, the Pt/C mass fraction becomes

$f = 10 \ Mass\%$ (Pt/C) using the base value of $m_C = 4.5 \ mg \ cm^{-2}$. Fig. 4 depicts the polarization curves and demonstrates that our computations match very well with the previously published results in both cases. The breakdown of losses (in terms of activation and ohmic losses) is also shown in Fig. 5, where according to Eq. 45 the sum of the losses subtracted from the reversible cell voltage gives V_{cell}.

6.2 Parametric Studies

We next perform a detailed parametric study of the effect on activation potential of changes in the following parameters: (i) platinum mass loading per unit area, m_{Pt}; (ii) carbon mass loading per unit area, m_C; (iii) volume fraction of ionomer phase, $L_{m,c}$; (iv) volume fraction of GDL material penetrating the CL, $L_{g,c}$; (v) GDL porosity, ε_g; and (vi) CL thickness l_c. The parameters are grouped in pairs and the results are summarized in the next three sections.

6.2.1 Effect of $L_{g,c}$ and $L_{m,c}$

In this section, we study the effect of changes in GDL and ionomer volume fractions on cell performance. In fact, when the MEA is synthesized there is ideally no penetration of the GDL into the CL; however, after the cell is assembled the MEA comes under a compressive load which can cause the GDL to penetrate into the catalyst. If the GDL is composed of a flexible carbon cloth material such as we consider in this study, it may experience large deformations into the gas channels etched in bipolar plates as well as significant penetration into the CL. We note that the observed degree of GDL penetration is not very large, with $L_{g,c}$ lying in the range of $5 \leq L_{g,c} \leq 15 \ Vol.\%$.

Fig. 6 shows the variation of activation overpotential with $L_{g,c}$ and $L_{m,c}$ for different values of platinum mass fraction f (where we have actually varied m_C to effect changes in f). The vertical axes are chosen identical in both plots so that it is obvious that the effect of changes in GDL fraction are much larger than for the membrane fraction. In Fig. 6-(Left), the curves increase slightly (i.e., performance degrades) with increases in $L_{g,c}$ primarily because of the increase in CL porosity ε_c and corresponding decrease in $D_{O_2}^{eff}$. On the other hand, as f increases the activation overpotential falls (and hence performance improves) since the specific area of the reaction sites (a) increases with f (see Eq. 32).

From the corresponding curves for ionomer volume fraction in Fig. 6-(Right), the activation overpotential actually decreases with increasing $L_{m,c}$. This can be explained by observing that ε_c (and hence also $D_{O_2}^{eff}$) decreases with increasing $L_{m,c}$ (see Eq. 10). On the other hand, the protonic conductivity κ^{eff} increases with $L_{m,c}$ according to Eq. 37, so that changes in $L_{m,c}$ have two opposing influences on CL performance with the net effect being to reduce η_{act} as $L_{m,c}$ increases.

6.2.2 Effect of m_{Pt} and m_C

The two plots in Fig. 7 depict the variation of activation overpotential in response to changes in platinum mass fraction f for different values of m_{Pt} and m_C. For f lying within the interval $[0.1, 0.3]$, variations in η_{act} are about the same magnitude; however, the activation overpotential is more sensitive to m_C than m_{Pt}. These simulations predict that the best CL performance occurs for the largest value of $f = 30 \, Mass\%$.

We focus first on changes in m_{Pt} shown in Fig. 7-(Left), where we observe that for all values except the largest $(m_{Pt} = 0.6 \, mA \, cm^{-2})$ the activation overpotential decreases monotonically with f. Also, the performance is less sensitive to m_{Pt} at larger f values, say when $f \geq 20 \, Mass\%$. In fact, increasing f has two competing effects on CL performance:

Effect 1: As f increases over the $[0.1, 0.3]$, the reaction surface area A_s decreases according to Eq. 33, which leads to a corresponding decrease in a (from Eq. 32). This has a negative influence on CL performance.

Effect 2: On the other hand, when m_{Pt} is held constant as f increases, the carbon loading m_C must decrease according to the definition $f = m_{Pt}/(m_{Pt} + m_C)$; that is, the contribution of the solid carbon particles within the CL decreases. This results in an increase in both CL porosity ε_c (see Eq. 10) and hence also oxygen diffusivity $D_{O_2}^{eff}$, which in turn improves CL performance.

These two effects therefore compete with each other with the net result being that η_{act} decreases with f as shown in Fig. 7-(Left).

Next we consider the right hand plot in Fig. 7, where curves of constant m_C decrease with increasing f. Analogous to the argument used for the m_{Pt} curves above, there are two competing effects on CL performance with the net result that increasing f improves performance. On the other hand, increasing the carbon loading (while holding f fixed) results in a decrease in performance owing to the presence of less platinum.

6.2.3 Effect ε_g and l_c

The two plots in Fig. 9 depict the variation of η_{act} with m_{Pt} and show that CL performance increases with m_{Pt}, which is primarily due to the fact that the specific area of reaction sites a also increases. The left hand plot includes curves for several values of GDL porosity, from which it is clear that the activation overpotential is relatively insensitive to changes in ε_g.

Fig. 9-(Right) shows the effect of changes in CL thickness on performance. In contrast with the ε_g plots, we see here much more significant variation from one curve to the next. Indeed, as the CL thickness l_c (or equivalently, the carbon loading m_C) is increased, there is a considerable drop in performance owing to increased ohmic losses. The variations in m_{Pt} along each curve correspond to

values of f ranging between 10–50 $Mass\%$, where points A, B and C refer to values of $f = 10$, 30 and 50 respectively.

It is important to note here that increasing the platinum loading is not the best way to optimize performance. Indeed, beyond the point B identified on the $m_{Pt} - \eta_{act}$ curves in Fig. 9-(Right) (corresponding to $f = 30$), the slope of the curve becomes so small that further efforts to increase platinum loading are not likely to lead to any significant improvment when considered in terms of a cost/benefit analysis. Similar conclusions were drawn by Cho et al. [29] in an experimental study using X-ray diffraction and cyclic voltametry measurement techniques. Instead, the best results are likely to be obtained using a multi-parameter design optimization which combines an efforts to increase Pt mass fraction with reductions in CL thickness.

7   Concluding Remarks

A comprehensive parametric study of CL performance was carried out by investigating the effects on activation overpotential of variations in six structural parameters: m_{Pt}, m_C, $L_{m,c}$, $L_{g,c}$, ε_g and l_c. The underlying mathematical model consists of a system of coupled nonlinear ODEs governing diffusion, electrochemical reactions and ohmic losses (given by Eqs. 28, 29 and 36). These equations, subjected to the boundary conditions given in Sec. 4, are solved using a shooting algorithm. The highlights of the results are summarized below:

- The effect of changes in the six parameters can be interpreted more easily by using two key intermediate parameters: namely, the specific area of the reaction sites a and CL porosity ε_c. In general, increasing either a or ε_c leads to improvements in performance.

- The results of the parameter study are summarized in Table 1 in terms of the range, optimum value, and sensitivity for each parameter considered. The parameters are also ranked from 1 to 6 in order of their importance, with the rank 1 for $L_{m,c}$ indicating that it is the structural parameter that has the most significant influence on CL performance. We note that the optimum

Table 1: Summary of the results for the parametric study.

Rank	structural parameter	ranges studied	optimum value	sensitivity $(\Delta\eta_{act}$ / V$)$
1	$L_{m,c}$ / $Vol.\%$	$10 - 50$	50	0.35
2	l_c / μm	$10 - 50$	10	0.07
3	m_C / $mg\,cm^{-2}$	$2 - 4$	2	0.025
4	m_{Pt} / $mg\,cm^{-2}$	$0.4 - 0.6$	0.4	0.015
5	$L_{g,c}$ / $Vol.\%$	$5 - 15$	5	0.01
6	ε_g / $Vol.\%$	$30 - 50$	50	≈ 0

performance is achieved in all cases at one of the endpoints of the range for the corresponding parameter.

- We observe the best performance in a narrow band of m_{Pt}, and for values outside of this range any increase in platinum loading is probably not economically justifiable. Similarly, Figs. 6 and 7 demonstrated that the best performance occurs at the highest value of platinum mass fraction f; however, the cost-to-benefit ratio drops significantly above a value of $f \approx 30\,Mass\%$.

- Most computations indicate that the bulk of the electrochemical reactions occur within a very thin layer close to the GDL boundary when current density $I_\delta > 50\,mA\,cm^{-2}$, since the oxygen gas dissolved in the ionomer penetrates only a small distance into the CL (see Fig. 3). This result suggests that the catalyst may be under-utilized (i.e., 10% or less of the CL thickness l_c is active) at normal operating cell current densities. Therefore, future efforts in catalyst layer design should be focused on thinner layers which will only improves platinum utilitization but also reduces ohmic losses.

Acknowledgement

References

[1] T. Berning, N. Djilali (2003) J Power Sources 124:440.

[2] K.W. Lum, J.J. McGuirk (2005) J Power Sources 143:103.

[3] W. Tiedemann, J. Newman (1975) J Electrochem Soc 122:1482.

[4] C. Marr, X. Li (1999) J Power Sources 77:17.

[5] L. You, H. Liu (2001) Int J of Hydrogen Energy 26:991.

[6] C.Y. Du, G.P. Yin, X.Q. Cheng et al (2006) J Power Sources 160:224.

[7] S.J. Ridge, R.E. White, Y. Tsou et al (1989) J Electrochem Soc 136:1902.

[8] M. Secanell, K. Karan, A. Suleman et al (2007) Electrochimica Acta 52:6318.

[9] A.A. Shah, G.S. Kim, P.C. Sui et al (2007) J Power Sources 163:793.

[10] G. Wang, P.P. Mukherjee, C.Y. Wang (2007) Electrochimica Acta 52:6367.

[11] E.A. Ticianelli, C.R. Derouin, A. Redondo et al (1988) J Electrochem Soc 135:2209.

[12] M. Javaheri (2009) Investigation of Synergism Effect of Carbon Nanotube in Catalyst Layer at Gas Diffusion Electrode of PEMFC, PhD. thesis, Tarbiat Modarres University, Iran.

[13] P.C. Sui, L.D. Chen, J.P. Seaba et al (1999) SAE SP–1425, Fuel Cell for Transportation, SAE, 1999–01–0539.

[14] D. Cheddie, N. Munroe (2005) Proceedings of The COMSOL Multiphysics User's Confrences, Boston.

[15] F.P. Incropera, D.P. De Witt (2006) Fundamentals of Heat and Mass Transfer, 6th ed. Wiley, New York.

[16] R.E. De la Rue, C.W. Tobias (1959) J Electrochem Soc 106:827.

[17] R.H. Perry, D.W. Green (1997) Chemical Engineers Handbook, 7th ed. McGraw-Hill.

[18] A. Parthasarathy, S. Srinivasan, A.J. Appleby (1992) J Electrochem Soc 139:2530.

[19] F. Barbir (2005) PEM Fuel Cells: Theory and Practice, University of California, Davis, Elsevier Academic Press.

[20] E-TEK (1995) Gas Diffusion Electrodes and Catalyst Materials, Catalogue.

[21] D.M. Bernardi, M.W. Verbrugge (1991) AIChE J 37:1151.

[22] J. Newman, K.E. Thoma-Alyea (2004) Electrochemical Systems, 3rd ed. Wiley, New York.

[23] C.F. Gerald, P.O. Wheatley (1999) Applied Numerical Analysis, 6th ed. Addision-Wesley.

[24] D.M. Bernardi, M.W. Verbrugge (1992) J Electrochem Soc 139:2477.

[25] C.L. Marr (1996) Performance Modeling of a Proton Exchange Membrane Fuel Cell, MSc. Thesis, University of Victoria, Canada.

[26] V.R. Chilukuri (2004) Steady State 1D Modeling of PEM Fuel Cell and Characterization of Gas Diffusion Layer, MSc. Thesis, Mississippi State University, USA.

[27] M. Khakbaz Baboli, M.J. Kermani (2008) Electrochimica Acta 53:7644.

[28] H.R. Shabgard (2006) Investigation and Analysis of the Condensation Phenomena in the Cathode Electrode of PEM Fuel Cells, MSc. thesis, Amirkabir University of Technology (Tehran Polytechnic), Iran.

[29] Y.H. Cho, H.S. Park, Y.H. Cho et al (2007) J Power Sources 172:89.

Table 2: Operational and structural parameters used for the base-case condition

| Parameters	Notation	Value
Temperature, ^oC	T	80
Gas mixture pressure, atm	P	5
Oxygen mole fraction	x_{O_2}	0.21
CL thickness, $\mu\, m$	l_c	50
Cell current density, $mA\ cm^{-2}$	I_δ	500
GDL porosity, $Vol.\%$	ε_g	40
Volume fraction of membrane in the CL, $Vol.\%$	$L_{m,c}$	40
Volume fraction of GDL in the CL, $Vol.\%$	$L_{g,c}$	10
Mass loading of platinum per unit area of the cathode, $mg\ cm^{-2}$	m_{Pt}	0.5
Mass loading of carbon per unit area of the cathode, $mg\ cm^{-2}$	m_C	4.5
Platinum density, $kg\ m^{-3}$	ρ_{Pt}	21400
Carbon density, $kg\ m^{-3}$	ρ_C	1800
Reference oxygen concentration, $mol\ m^{-3}$	$C_{O_2,ref}$	1.2
Cathodic transfer coefficient	α_c	1
Anodic transfer coefficient	α_a	0.5
Bulk protonic conductivity, $(\Omega\, m)^{-1}$	κ	17
Bulk electronic conductivity, $(\Omega\, m)^{-1}$	σ	7.27×10^4
Oxygen diffusion coefficient within the liquid water, $m^2\ s^{-1}$	D_{O_2-W}	9.19×10^{-9}
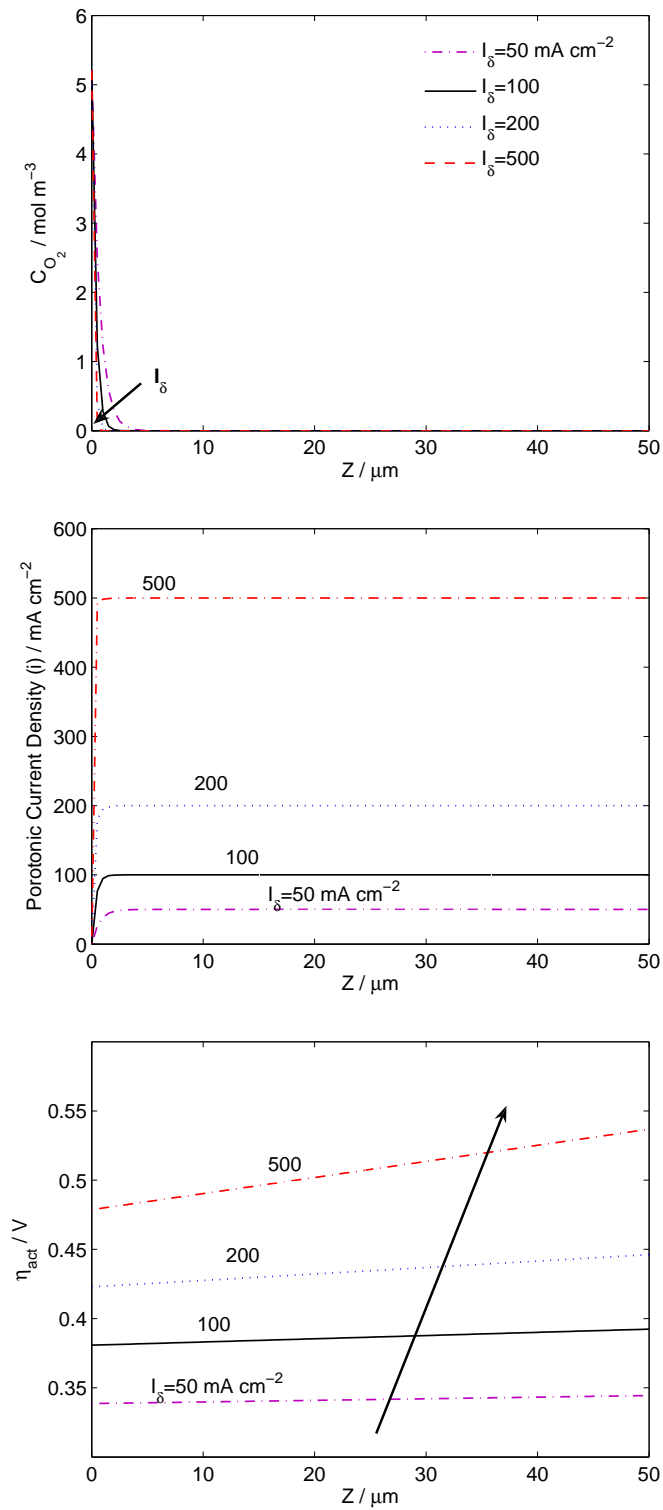
Figure 3: Sample of base case computations at four cell current densities in terms of oxygen concentration C_{O_2} (top), protonic current density i (middle), and activation overpotential η_{act} (bottom).
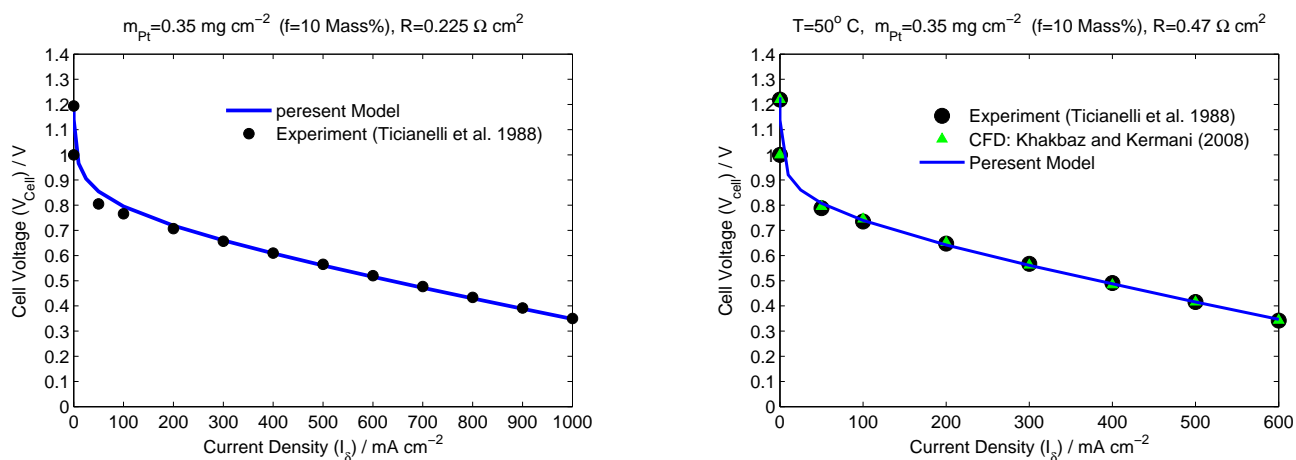
Figure 4: Comparisons of polarization curve from the our numerical simulations with two different published results: (Left)- experiments of Ticianelli et al. (1988), using the base case parameters except with $m_{Pt} = 0.35\,mg\,cm^{-2}$ ($f = 10$ Pt/C $Mass\%$) and $R = 0.225\,\Omega\,cm^{-2}$; (Right)- CFD computations of Khakbaz-Baboli and Kermani (2008) using the base case parameters except with $m_{Pt} = 0.35\,mg\,cm^{-2}$ ($f = 10$ Pt/C $Mass\%$), $R = 0.47\,\Omega\,cm^{-2}$ and $T = 50^{o}C$.
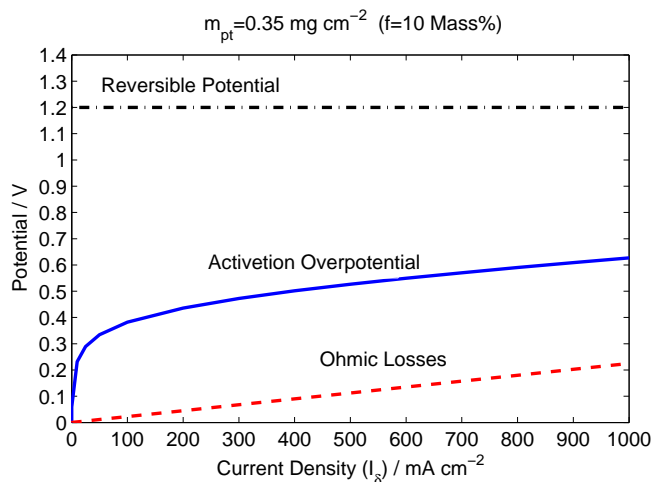
Figure 5: The break down of losses into activation overpotential and ohmic losses.
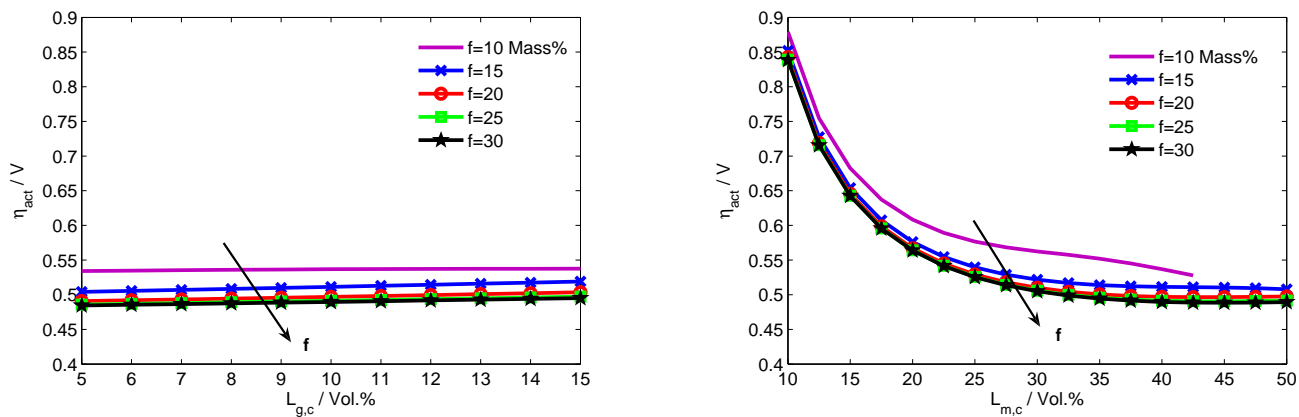
Figure 6: The variation in activation overpotential with $L_{g,c}$ (Left) and $L_{m,c}$ (Right) for different f values at the base case condition.
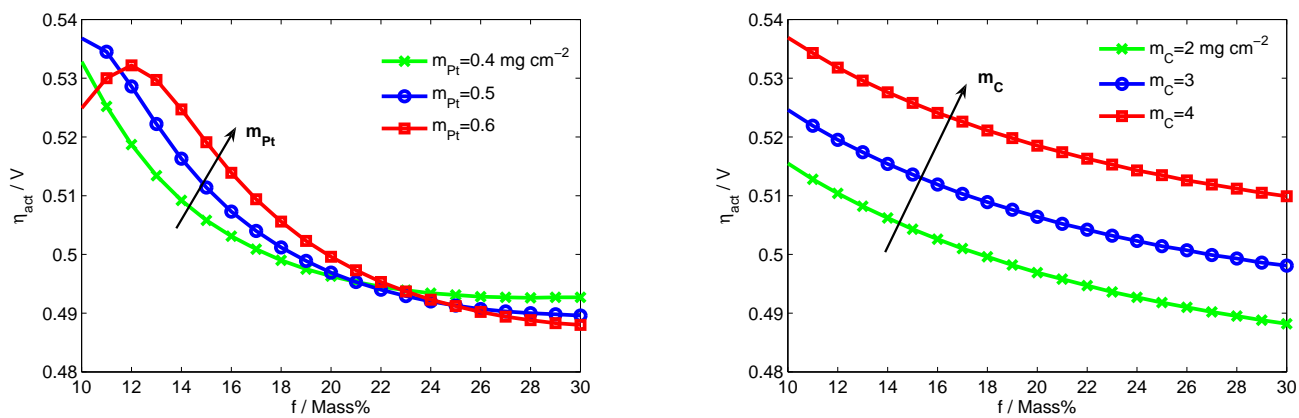

Figure 7: The variation in activation overpotential with f at the base case condition: (Left)- for different m_{Pt} values and (Right)- for different m_C values.

Manuscript Submitted to Journal of Applied Electrochemistry
Khajeh-Hosseini D., Kermani, Ghadiri Moghaddam and Stockie
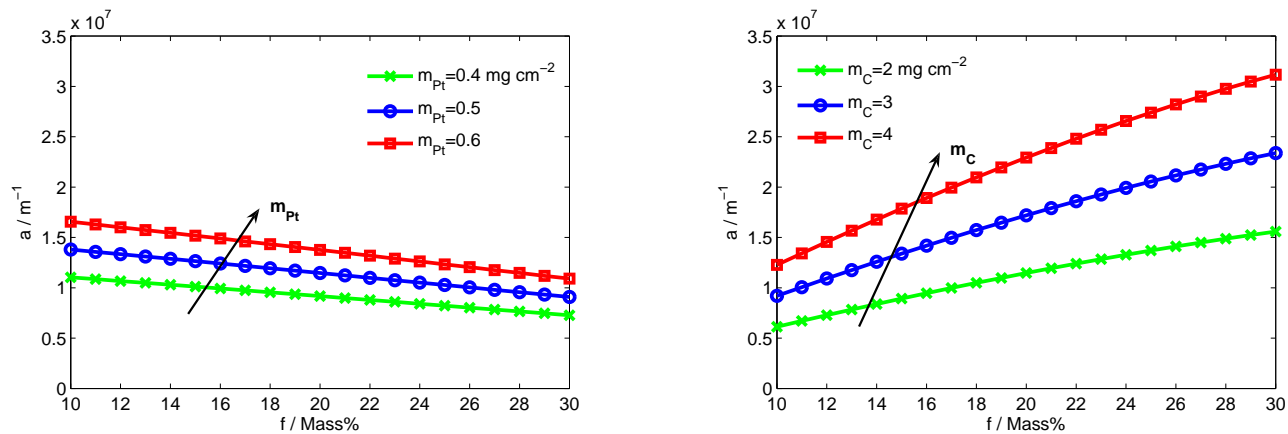
Figure 8: The variation in specific area of reaction sites with f at the base case condition: (Left)- at different m_{Pt} values and (Right)- at different m_C values.
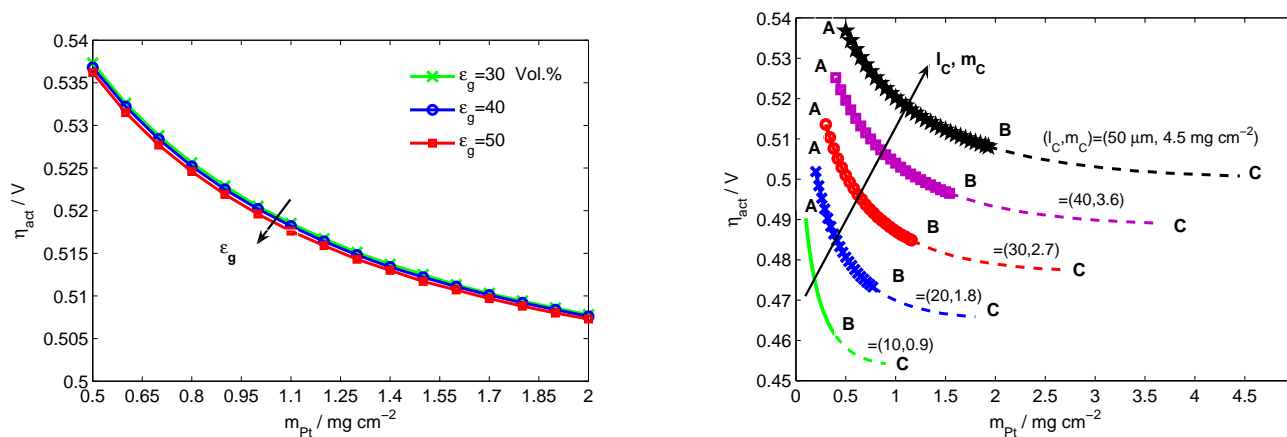

Figure 9: The variation in activation overpotential with m_{Pt} at the base case condition: (Left)- at different GDL porosity ε_g and (Right)- at different catalyst layer thicknesses l_c.